INTERNATIONAL JOURNAL FOR NUMERICAL METHODS IN FLUIDS
Int. J. Numer. Meth. Fluids 2006; **52**:63–88
Published online 10 February 2006 in Wiley InterScience (www.interscience.wiley.com). DOI: 10.1002/fld.1156

Continuous, discontinuous and coupled discontinuous–continuous Galerkin finite element methods for the shallow water equations

Clint Dawson[1], Joannes J. Westerink[2,*,†], Jesse C. Feyen[2] and Dharhas Pothina[1]

[1]*Institute for Computational Engineering and Sciences, University of Texas, Austin, TX 78712-1528, U.S.A.*
[2]*Department of Civil Engineering and Geological Sciences, University of Notre Dame, Notre Dame, IN 46556-5602, U.S.A.*

SUMMARY

We consider the approximation of the depth-averaged two-dimensional shallow water equations by both a traditional continuous Galerkin (CG) finite element method as well as two discontinuous Galerkin (DG) approaches. The DG method is locally conservative, flux-continuous on each element edge, and is suitable for both smooth and highly advective flows. A novel technique of coupling a DG method for continuity with a CG method for momentum is developed. This formulation is described in detail and validation via numerical testing is presented. Comparisons between a widely used CG approach, a conventional DG method, and the novel coupled discontinuous–continuous Galerkin method illustrates advantages and disadvantages in accuracy and efficiency. Copyright © 2006 John Wiley & Sons, Ltd.

KEY WORDS: shallow water equations; Galerkin finite element method; discontinuous Galerkin method; coupled finite element method

1. INTRODUCTION

The shallow water equations (SWE) model flow in domains whose characteristic wave length in the horizontal is much larger than the water depth [1]. Simulation of flow in shallow waters can be used, for example, to model environmental effects of dredging and commercial activities on fisheries and coastal wildlife, remediation of contaminated bays and estuaries for

*Correspondence to: Joannes J. Westerink, Department of Civil Engineering and Geological Sciences, University of Notre Dame, 156 Fitzpatrick Hall, Notre Dame, IN 46556-5602, U.S.A.
†E-mail: jjw@nd.edu

Contract/grant sponsor: National Science Foundation; contract/grant number: DMS-0107247
Contract/grant sponsor: U.S. Army Engineer Research and Development Centre; contract/grant number: DACW 42-00-C-0006

Received 28 January 2004
Revised 22 October 2005
Accepted 25 October 2005

the purposes of improving water quality, modelling the effects of storm surges due to tropical storms and hurricanes, and studying freshwater–saltwater interactions.

The SWE consist of a first-order hyperbolic continuity equation for the water elevation, coupled to momentum equations for the horizontal depth-averaged velocities. This system is referred to as the primitive form of the SWE. These equations are often solved on domains with fairly irregular coastal boundaries. Furthermore, to avoid spurious boundary effects, it is often desirable to extend the domain away from the shore into deeper waters [2, 3].

Various finite element approaches have been developed for solving the SWE on such complex domains over the past two decades; see, for example, References [4–8]. Much of this effort has been directed at deriving a finite element method which is stable and non-oscillatory under highly varying flow regimes, including advection dominant flows. As noted in Reference [4], a straightforward use of equal order approximating spaces for elevation and velocity in the primitive SWE can lead to spurious spatial oscillations. Approaches based on mixed interpolation spaces [5] have met with limited success. A more widespread approach has been to replace the first-order hyperbolic elevation equation with a second-order hyperbolic 'wave continuity equation', first proposed in Reference [4]. This model was extended to the generalized wave continuity equation (GWCE) in Reference [9]. This approach has been utilized in numerous finite element studies, see for example References [2, 3, 10–19], and was analysed in References [20, 21]. This formulation is also the basis for the advanced circulation (ADCIRC) model [14], developed by the second author and several collaborators.

The finite element methods mentioned above are based on continuous approximating spaces. In recent years, finite element methods based on discretizing the primitive form of the SWE using discontinuous approximating spaces have been studied [22–27]. This discontinuous Galerkin (DG) approach has several appealing features; in particular, the ability to incorporate upwinding and stability post-processing (slope-limiting) into the solution to model highly advective flows, the ability to use different polynomial orders of approximation in different parts of the domain, and the ability to easily use non-conforming meshes (e.g. with hanging nodes). Moreover, the DG method is 'locally conservative' and 'flux-continuous', that is, the continuity equation relating the change in water elevation to water flux is satisfied in a weak sense, element-by-element, and the numerical flux over each inter-element edge or face is continuous. These properties are useful when coupling the SWE to a transport equation for modelling, for example, contaminant migration [28]. The GWCE formulation sacrifices the primitive continuity equation, thus the primitive form is no longer satisfied in a discrete sense. This implies and has led to continuity imbalances. DG methods have proven adept at modelling hyperbolic equations [29–34], advection–diffusion [35–38] and pure diffusion equations [39–43]. See also Reference [44] for a more thorough discussion on the history of DG methods. The disadvantage of DG methods over standard Galerkin methods is their cost: typically they require more degrees of freedom on a fixed mesh than their continuous counterparts. The DG method is the basis of the University of Texas Bay and Estuary (UTBEST) simulator [23, 24], developed by the first author and collaborators.

In this paper, we present a new approach for the SWE based on combining a DG method for continuity with a standard continuous Galerkin (CG) method for momentum. This approach allows us to model the hyperbolic continuity equation using the DG method, which is well-suited for this type of equation, while still using a continuous method for momentum. Therefore, we reduce the overall degrees of freedom using a complete DG method as in Reference [24] while retaining a locally conservative, flux continuous solution to the continuity

equation. Stability and convergence results for this new methodology have recently been derived in Reference [45]. Here we will focus on the numerical implementation of the method and its validation by numerical test problems. We also compare this formulation to results from ADCIRC and UTBEST. Application of the methodology can be seen in Reference [46], which in particular discusses important issues pertaining to mass balance properties and the impact of slope limiting.

We have implemented this new approach into ADCIRC. ADCIRC discretizes both the GWCE and the momentum equation using continuous, piecewise linear approximating functions defined on triangular elements. The GWCE is a quite complex and cumbersome method, owing to the replacement of the first-order hyperbolic continuity equation with a second-order hyperbolic equation. The GWCE finite element formulation also does not produce a locally conservative, flux-continuous solution to the continuity equation. Moreover, the GWCE has no particular mechanism for handling highly advective flows, such as upwinding or stabilization. The GWCE does work very well for smooth tidal flows; see References [10, 11, 13, 16]. In our implementation, we have essentially replaced the GWCE formulation with a DG method.

The paper is organized as follows. In the following section, we describe the mathematical model and the numerical approximation. Section 3 then contains numerical results for the two-dimensional quarter annular test problem.

2. PROBLEM DEFINITION

Vertical integration of the Navier–Stokes equations along with the assumptions of a hydrostatic pressure and a vertically uniform horizontal velocity profile results in the SWE of the following form:

$$\mathscr{L} \equiv \frac{\partial \xi}{\partial t} + \nabla \cdot (\mathbf{u}H) = 0 \tag{1}$$

$$\frac{\partial \mathbf{u}}{\partial t} + \mathbf{u} \cdot \nabla \mathbf{u} + \tau_{\mathrm{bf}}(\mathbf{u})\mathbf{u} + f_{\mathrm{c}}\mathbf{k} \times \mathbf{u} + g\nabla\xi - \mathbf{F} = 0 \tag{2}$$

Equation (1) represents the conservation of mass and is also referred to as the primitive continuity equation; (2) represents the conservation of momentum in non-conservative form. The 'conservative form' of the momentum equations is obtained by multiplying (2) by H and applying (1) to obtain

$$\mathscr{M} \equiv \frac{\partial \mathbf{Q}}{\partial t} + \nabla \cdot (\mathbf{Q}\mathbf{Q}/H) + \tau_{\mathrm{bf}}(\mathbf{u})\mathbf{Q} + f_{\mathrm{c}}\mathbf{k} \times \mathbf{Q} + gH\nabla\xi - \mathbf{F} = 0 \tag{3}$$

where $\mathbf{Q} = \mathbf{u}H$.

In the above equations, ξ represents the deflection of the air–water interface from the mean sea level, $H = h_{\mathrm{b}} + \xi$ represents the total fluid depth, and h_{b} is the bathymetric depth, $\mathbf{u} = (u, v)$ is the depth averaged horizontal velocity field, f_{c} is the Coriolis parameter resulting from the earth's rotation, $\mathbf{k}$ is the local vertical vector, g is the gravitational acceleration, τ_{bf} is the bottom friction coefficient. Here we have neglected second-order derivative terms in the momentum equation due to turbulent viscosity. In addition to the above-described phenomena,

often we need to include the effects of surface wind stress, variable atmospheric pressure and tidal potential forcing which are expressed through the body force **F** [1].

These equations are solved over a spatial domain Ω in $\mathbb{R}^2$ and for time $t>0$. Let $\partial\Omega$ denote the boundary of Ω, where **n** is the fixed unit outward normal to $\partial\Omega$. Specified elevation and velocity and/or specified fluxes are assumed on $\partial\Omega$. Initial elevations and velocities ξ^0 and $\mathbf{u}^0$ at $t=0$ must also be given.

In order to formulate finite element methods for the above system, let $\{\mathscr{T}_h\}_{h>0}$ denote a triangulation of Ω such that no triangle Ω_e crosses $\partial\Omega$. We assume each element Ω_e has an element diameter h_e, with h being the maximal element diameter.

2.1. The GWCE and ADCIRC methodology

The GWCE is obtained by differentiating (1) with respect to time, (3) with respect to space, adding the result, and adding a parameter τ_0 times (1). In operator notation, this can be written as

$$\mathscr{L}_t + \nabla\cdot\mathscr{M} + \tau_0\mathscr{L} = 0 \tag{4}$$

It is important to note that the basic first-order hyperbolic continuity equation has been removed and is no longer satisfied. The replacement GWCE equation has the benefit of a non-folded dispersion relationship when subject to a CG discretization, but does not satisfy continuity. Furthermore, it is more complex and is difficult to adequately analyse, and its performance is subject to selection of τ_0.

A weak formulation of (4)–(2) is obtained by multiplying each equation by smooth test functions, integrating over Ω and integrating certain terms by parts. In ADCIRC, ξ and **u** are both approximated by continuous, piecewise linear functions determined through this weak formulation, see Reference [14].

2.2. The DG method and UTBEST

UTBEST is based on multiplying (1)–(3) by (possibly) discontinuous test functions, and integrating over a single element Ω_e. This DG formulation gives rise to a flux term on the boundaries between elements. This flux term is approximated using the so-called Roe numerical flux, described in Reference [23].

In UTBEST, both ξ and **Q** are approximated by discontinuous, piecewise polynomials of some degree k, defined on each element Ω_e. In our implementation we have considered constants ($k=0$), linears ($k=1$) and quadratics ($k=2$).

2.3. A coupled DG/CG method

In this section, we describe a new method based on combining the DG method for the primitive continuity equation (1) with a CG finite element method for the momentum equation (2).

In order to describe the method, we first define some notation. Let $\mathscr{P}^k(\Omega_e)$ denote the space of complete polynomials of degree $k\geqslant 0$, defined on Ω_e. For any function $v\in H^1(\Omega_e)$, for each element Ω_e, we denote its trace on interior edges γ_{i} by $v^{\pm}$, with

$$v^-(\mathbf{x}) = \lim_{s\to 0-} v(\mathbf{x}+s\mathbf{n}_{\mathrm{i}}), \quad v^+(\mathbf{x}) = \lim_{s\to 0+} v(\mathbf{x}+s\mathbf{n}_{\mathrm{i}})$$

where $\mathbf{x} \in \gamma_i$ and $\mathbf{n}_i$ denotes a fixed unit vector normal to γ_i, see Figure 1. We will use the $L^2(R)$ inner product notation $(\cdot,\cdot)_R$ for domains $R \in \mathbb{R}^2$, and the notation $\langle u, v\rangle_R$ to denote integration over one-dimensional surfaces.

Multiply Equation (1) by an arbitrary test function $v \in H^1(\Omega_e)$ and integrate by parts over each element Ω_e to obtain

$$(\partial_t \xi, v)_{\Omega_e} - (\mathbf{u}H, \nabla v)_{\Omega_e} + \langle H\mathbf{u}\cdot\mathbf{n}_e, v\rangle_{\partial\Omega_e} = 0 \tag{5}$$

where $\mathbf{n}_e$ denotes the outward unit normal to the edge $\partial\Omega_e$.

Multiply Equation (2) by a test function $\mathbf{w} \in (H^1(\Omega))^2$ and integrate over Ω to obtain,

$$\left(\frac{\partial \mathbf{u}}{\partial t} + \mathbf{u}\cdot\nabla\mathbf{u} + \tau_{\mathrm{bf}}(\mathbf{u})\mathbf{u} + f_c\mathbf{k}\times\mathbf{u} + g\nabla\xi, \mathbf{w}\right)_\Omega = (\mathbf{F}, \mathbf{w})_\Omega \tag{6}$$

We approximate ξ in the polynomial space $V_h = \{v : v|_{\Omega_e} \in \mathscr{P}^k(\Omega_e)\}$, and we approximate each component of $\mathbf{u}$ in the subspace W_h of $H^1(\Omega)$, where W_h consists of continuous, piecewise linear polynomials. Denote these approximations by ξ_h and $\mathbf{u}_h$. We also will utilize a continuous approximation $\pi\xi_h \in W_h$ to ξ, defined below.

In continuous time, the DG/CG scheme is outlined as follows:

- First, initial approximations $\xi_h(\cdot,0) \in V_h$ and $\mathbf{u}_h(\cdot,0) \in (W_h)^2$ are computed from the initial data ξ^0 and $\mathbf{u}^0$. This can be done by interpolation or L^2 projection.
- For $t > 0$, ξ_h is computed by

$$(\partial_t \xi_h, v)_{\Omega_e} - (\mathbf{u}_h(\xi_h + h_b), \nabla v)_{\Omega_e} + \langle \mathbf{A}(\mathbf{u}_h; \xi_h^-, \xi_h^+)\cdot\mathbf{n}_e, v\rangle_{\partial\Omega_e} = 0, \quad v \in V_h \tag{7}$$

The numerical flux $\mathbf{A}(\mathbf{u}_h; \xi_h^-, \xi_h^+)\cdot\mathbf{n}_e \approx H\mathbf{u}\cdot\mathbf{n}_e$. We will discuss this term in detail below.

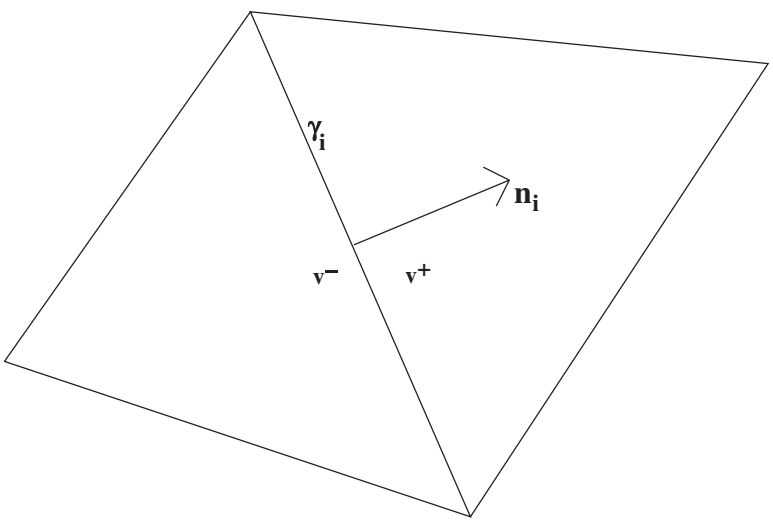

Figure 1. An edge γ_i with normal vector $\mathbf{n}_i$; v^- and v^+ are the values of v to the left and right of the edge, as determined by the normal $\mathbf{n}_i$.

- ξ_h is then projected into the continuous space W_h by finding $\pi\xi_h \in W_h$ satisfying

$$(\pi\xi_h, w)_\Omega = (\xi_h, w)_\Omega, \quad w \in W_h \tag{8}$$

  In our implementation, mass lumping is used to approximate the integral on the left side of (8). Furthermore, on elevation specified boundary nodes, we set $\pi\xi_h$ to be equal to the specified elevation.
- Finally $\mathbf{u}_h$ is computed from (6) by

$$\left(\frac{\partial \mathbf{u}_h}{\partial t} + \mathbf{u}_h \cdot \nabla \mathbf{u}_h + \tau_{\mathrm{bf}}(\mathbf{u}_h)\mathbf{u}_h + f_c \mathbf{k} \times \mathbf{u}_h + g\nabla\pi\xi_h, \mathbf{w}\right)_\Omega = (\mathbf{F}, \mathbf{w})_\Omega, \quad \mathbf{w} \in (W_h)^2 \tag{9}$$

Note that (7) is conservative in the following sense: letting $v = 1$ on Ω_e and zero elsewhere, we find

$$\int_{\Omega_e} \partial_t \xi_h \, \mathrm{d}x + \int_{\partial\Omega_e} \mathbf{A}(\mathbf{u}_h; \xi_h^-, \xi_h^+) \cdot \mathbf{n}_e \, \mathrm{d}s = 0 \tag{10}$$

Thus, the change in elevation is balanced by the numerical flux $\mathbf{A} \cdot \mathbf{n}_e$ through the boundary of the element. As we will see below, this flux is uniquely defined (i.e. continuous) on each edge in the mesh. Thus, the DG scheme is both 'locally conservative' and 'flux continuous.'

We now describe in more detail the implementation of the scheme above.

Implementation of (7). Though (7) is valid for any polynomial degree $k \geqslant 0$, we have implemented polynomials of order $k = 0$ and 1. For $k = 1$, we write

$$\xi_h|_{\Omega_e} \equiv \xi_{h,e} + \delta_x \xi_{h,e}(x - x_e) + \delta_y \xi_{h,e}(y - y_e) \tag{11}$$

where (x_e, y_e) is the barycentre of Ω_e. Thus, there are three degrees of freedom for ξ_h per element, and the basis functions for $\mathscr{P}^1(\Omega_e)$ are

$$\{1, x - x_e, y - y_e\}$$

For $k = 0$, the x and y slope terms are omitted.

The time discretization of (7) is explicit. Given a time step $\Delta t > 0$ and initial approximations $(\xi_h(\cdot, t^n), \mathbf{u}_h(\cdot, t^n)) \equiv (\xi_h^n, \mathbf{u}_h^n)$, we integrate (7) forward in time using the explicit Euler method if $k = 0$, and using a second-order Runge–Kutta method if $k = 1$. The second-order Runge–Kutta method consists of computing two successive explicit Euler approximations, $\xi_h^{n,1}$ and $\xi_h^{n,2}$, keeping $\mathbf{u}_h^n$ fixed, and setting

$$\xi_h^{n+1} = \tfrac{1}{2}(\xi_h^n + \xi_h^{n,2}) \tag{12}$$

At each Euler step, a slope limiter is applied to the slope terms $\delta_x \xi_{h,e}$ and $\delta_y \xi_{h,e}$ to minimize any overshoot or undershoot. For an interior triangle Ω_e, with neighbouring triangles $\Omega_{e,1}$, $\Omega_{e,2}$ and $\Omega_{e,3}$, we interpolate the constant cell averages in Ω_e and each pair of neighbouring triangles by linears, as described in Reference [47], resulting in three linear interpolants on Ω_e. We compare these linear interpolants to that produced using the DG method. The interpolant with smallest gradient in magnitude is chosen as the linear approximation over the element. For elements Ω_e next to specified elevation boundaries, the boundary condition is utilized in the interpolation procedure. If Ω_e lies on land boundaries, we reflect the element and the

solution across the land boundary, and treat this reflected element as a neighbouring element in the interpolation process.

The numerical flux $A(\mathbf{u}_h; \xi_h^-, \xi_h^+)$ is evaluated using the Roe flux as described in detail in Reference [23]. This flux is an upwind flux which has been used in many fluid applications with shocks and sharp gradients. In Reference [23], we showed how to apply this flux when using a finite volume method (a DG method with $k=0$) for both continuity and momentum. Here we only need to apply it to the continuity equation. Thus, we are only interested in the first component of this flux, which on edge γ_i, is defined as follows:

$$\mathbf{n}_i = (n_i^x, n_i^y) = \text{ normal vector to } \gamma_i$$

$$H^{\pm} = \xi_h^{\pm} + h_b$$

$$\mathbf{q}^{\pm} = \mathbf{u}_h H^{\pm}$$

$$[\![H]\!] = H^+ - H^-$$

$$[\![\mathbf{q}]\!] = ([\![q^x]\!], [\![q^y]\!]) = \mathbf{q}^+ - \mathbf{q}^-$$

$$\hat{a} = \sqrt{g(H^- + H^+)/2}$$

$$\hat{\kappa} = \sqrt{H^+/H^-}$$

$$\hat{\mathbf{u}} = \frac{\mathbf{q}^-}{(H^-)(1+\hat{\kappa})} + \frac{\mathbf{q}^+}{(H^+)(1+1/\hat{\kappa})}$$

$$u_n = \hat{\mathbf{u}} \cdot \mathbf{n}_i$$

$$\lambda_1 = \min(u_n - \hat{a}, 0)$$

$$\lambda_2 = \min(u_n + \hat{a}, 0)$$

$$\alpha_1 = \frac{(\hat{a} + u_n)[\![H]\!] - [\![\mathbf{q}]\!] \cdot \mathbf{n}_i}{2\hat{a}}$$

$$\alpha_2 = \frac{(\hat{a} - u_n)[\![H]\!] + [\![q^x]\!]\mathbf{n}_i^x - [\![q^y]\!]\mathbf{n}_i^y}{2\hat{a}}$$

$$\mathbf{A}(\mathbf{u}_h; \xi_h^-, \xi_h^+) \cdot \mathbf{n}_i \equiv \mathbf{q}^- \cdot \mathbf{n}_i + \lambda_1\alpha_1 + \lambda_2\alpha_2$$

Note that, on any element, the outward normal $\mathbf{n}_e$ is either $\mathbf{n}_i$ or $-\mathbf{n}_i$, thus $\mathbf{A} \cdot \mathbf{n}_i$ is either $\mathbf{A} \cdot \mathbf{n}_e$ or $-\mathbf{A} \cdot \mathbf{n}_e$. Furthermore, if $k=0$, the midpoint rule is used to approximate the integral

$$\langle \mathbf{A} \cdot \mathbf{n}_e, w \rangle_{\partial\Omega_e}$$

That is, $\mathbf{u}_h, \xi_h^-$ and ξ_h^+ are evaluated at the midpoint of the edge in computing $\mathbf{A} \cdot \mathbf{n}_i$. If $k=1$, two point Gaussian quadrature is used. The integration of the other terms in (7) is exact, assuming that h_b is given as a continuous, piecewise linear interpolant of bathymetric data.

On elevation specified boundaries, the boundary condition is enforced through the flux $\mathbf{A} \cdot \mathbf{n}_e$ by setting ξ_h^+ equal to the specified elevation. On land boundaries, $\mathbf{A} \cdot \mathbf{n}_i$ is set to zero. On other boundaries, without any prior knowledge of ξ, we simply set $\xi_h^+ = \xi_h^-$.

Wetting and drying is implemented in (7) on each edge γ_i (unless this edge has already been designated a land edge). In particular, an edge is determined to be 'wet' if $H^+ + H^- > 0$

and 'dry' otherwise. For dry edges, we set $\mathbf{A} \cdot \mathbf{n}_i = 0$. For a wet edge, one of the elements on either side could be dry. If, for example, $H^+ \leqslant 0$, then we modify the computation of $\mathbf{A} \cdot \mathbf{n}_i$ by omitting the calculation of $\hat{\kappa}$, redefining $\hat{\mathbf{u}} = \mathbf{u}_h$, and proceeding with the calculations given above.

Implementation of (9). The implementation of the CG method (9) follows what has traditionally been done in ADCIRC [14]. In particular, mass lumping is employed in the first term, and mostly explicit time stepping is used, except that $\pi\xi_h$ is evaluated at the new time level t^{n+1}.

3. NUMERICAL TESTING

We evaluate the error and convergence properties of the coupled DG/CG method and compare it to the GWCE and DG methods in addition to examining the associated costs. In particular, we examine a weakly non-linear version of the widely used quarter annular harbour test case using four levels of grid resolution and three grid configurations. The quarter annular case was developed by Lynch and Gray [48] for testing of SWE algorithms. It is a convenient domain since tidal response is uniform across the θ direction, and numerical solutions should be as well. This uniformity also facilitates examination of spurious oscillations, as we can compare adjacent nodal values along each radius. An analytical solution to the linearized SWE exists for the domain [48]. The linearized SWE disregard advection and make a finite amplitude approximation ($H \simeq h$) in addition to linearizing bottom friction. However, the use of the linearized equations is not appropriate in this study for several reasons. First, the DG methodology is inherently designed to use the finite amplitude terms for incorporating elevation boundary condition forcing into the continuity equation through the flux term on element boundaries. Second, we desire to develop a SWE model that will perform well for advective flows, and therefore these terms should be included in numerical testing. We therefore test the SWE with non-linear advection and finite amplitude terms but we linearize the bottom friction terms. Since an analytical solution is not available for this form of the equations we generate a highly resolved 'truth' solution which is the basis of our error analysis.

In order to assess solution quality, errors in the harmonic amplitudes of the M_2 forcing constituent for elevation and velocity are determined via comparison to the highly accurate 'truth' solution. Additionally, spurious oscillations are examined in each solution. All tests are executed on four grid spacings so that a rigorous convergence study can be performed. All three methods apply linear approximating polynomials and should lead to second-order convergence within the interior of the domain for both elevation and velocity [45].

Boundary condition treatments differ between methods, and will affect solution quality in different ways. Therefore, we examine accuracy, oscillations, and convergence both over the entire domain and within a fixed interior portion of the domain in order to limit the influence of boundary conditions. At elevation-specified open ocean boundaries the GWCE method applies an essential boundary condition by replacing the GWCE with the elevation boundary condition value at all boundary nodes. Both the DG-based algorithms impose elevation boundary conditions weakly via the flux term, and use the Roe numerical flux approximation to compute the flux through the boundary. The weakly imposed flux boundary condition is only applied to the continuity equation in DG/CG but in DG is applied to both the continuity and momentum equations, and therefore specifies both the elevation and velocity boundary

conditions in a weak sense. The GWCE and DG/CG methods solve the momentum equation at elevation-specified boundaries using a one-sided approximation to the pressure gradient term. This leads to a first-order accurate approximation for the spatial gradient in elevation and degradation of the accuracy of the resulting velocity solution. At velocity-specified boundaries, the GWCE and DG/CG methods enforce an essential boundary condition by setting the normal flux term in the continuity equation to zero and eliminating the normal momentum equation. These essential boundary conditions can be considered to over-constrain the solution at velocity boundaries, but the effects of this are not well known. Note that only the DG method has the advantage of weak boundary conditions that do not affect accuracy of both the continuity and momentum equations as verified in References [38, 45].

In order to investigate the relative advantages of each method, comparisons of the computational costs are made and discussed. Wall clock run times for each of the numerical methods over a series of quarter annular grids are documented. The DG methodology leads to a larger number of degrees of freedom than does CG for a conforming mesh, leading to expected highest costs for the DG method and lowest for GWCE. While factors such as matrix assembly and coding efficiency also affect cost, there are inherent cost differences between methods.

3.1. Test case

The domain is formed from a quarter annulus with an outer radius 500 000 ft from the origin and an inner radius at 200 000 ft. The bathymetric profile increases quadratically from 10.0 ft at the inner radius to 62.5 ft at the outer radius. Flow is driven by a M_2 tidal forcing signal (period of 12.42 h) which is applied uniformly at the outer radius as an elevation-specified boundary condition. The tidal forcing amplitude is ramped up using a hyperbolic tangent function from 0 to 5 ft over the first 5 days of a 30 day run. The flow propagates from the outer radius towards the inner, and since the Coriolis effect is not considered, results along all angles (θ) at a given radius should be uniform. The remaining boundaries are treated as land boundaries which prevent normal flow. The GWCE uses essential conditions for all boundaries, specifying elevation at the forcing boundary and elsewhere a no-normal flow velocity boundary condition in both the GWCE flux integral and in the momentum equations (which may be over-constraining the system at velocity boundaries). The DG method uses weak boundary conditions, generated by way of the elemental flux integral terms. The DG/CG method is a combination of these two methods, using a weak boundary condition generated from the boundary integral in the continuity equation to consider elevation boundary conditions, and an essential condition for land boundaries that replaces the normal momentum equation with no-normal velocity response as well as sets the elemental flux integral to zero.

Weakly non-linear flow conditions are generated within the domain due to the quadratically varying bathymetry that becomes relatively shallow with respect to tidal response. Under the influence of the bathymetric gradient, advection and finite amplitude effects increase as depth decreases approaching the inner boundary, generating overtides at integer multiples of the forcing frequency within the inner half of the domain. It should be noted that they are at most 10% of the M_2 amplitude.

A linear bottom friction relationship is used and the friction term is set to a constant value of 0.0001. For the GWCE solutions, the numerical weighting parameter τ_0 is set to 0.0001, matching the bottom friction term. Eddy viscosity and Coriolis effects are not included. With these small viscous terms, this system has very little inherent damping.

There are three configurations of triangular finite element discretizations tested here. Atkinson *et al*. [49] have shown that these grid configurations can have different dispersion properties and therefore can exhibit differences in their solutions. Therefore, all three configurations are tested here to examine differences that may exist with each method. Figure 2 shows the 6eq grid, which is composed of six equilateral triangles about each node. The 6b grid, shown in Figure 3, has six triangles about each node which are constructed from

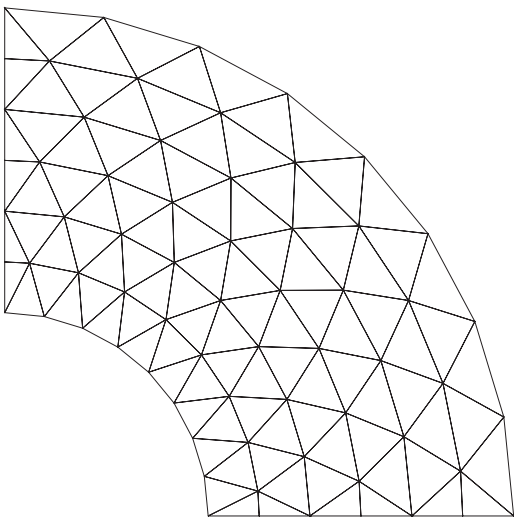

Figure 2. 6eq grid configuration.

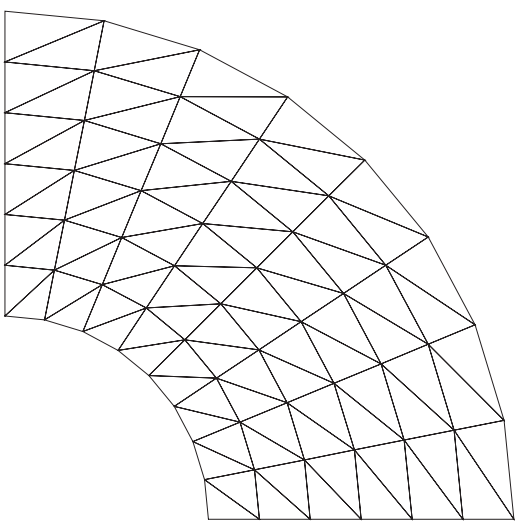

Figure 3. 6b grid configuration.

bisected quadrilaterals. The 4–8 grid (Figure 4) is composed of an alternating pattern of four and eight isosceles triangles grouped about each node.

In order to determine convergence behaviour, four levels of resolution were used for each grid configuration. The coarsest resolution has a nodal spacing of 50 000 ft measured in the direction of propagation. Resolution is increased by repeatedly halving grid spacing to 25 000, 12 500, and 6250 ft. In order to ensure that spatial errors are dominant, a time step of 5.0 s is used for the two coarsest grids, and 2.5 s for the two finest grids. Under these conditions the time step versus nodal spacing relationship corresponds to maximum celerity-based Courant values of 0.0045, 0.0090, 0.0090, and 0.018 for the four grids. A GWCE solution on a highly refined grid with a nodal spacing of 1562.50 ft (one quarter of the finest grid) and a time step of 0.5 s is used as a 'truth' solution. This highly refined solution is used to compute the accuracy of the GWCE, DG, and DG/CG schemes and check the convergence rate. Errors were also computed using a Richardson-based error extrapolation procedure which does not rely on any 'truth' solution but instead compares results over a range of grid spacings [50]. Those results are very similar and confirm what is found using the 'truth' solution and thus are omitted here for brevity.

Model output is harmonically decomposed over the final 10 days of each run in order to perform the error analyses. The elevation and radial velocity time series are decomposed into tidal amplitude and phase information at each nodal location for the M_2 constituent and its overtides. In order to compute the error measures, the M_2 constituent is separated into sine and cosine components for elevation and velocity. These components of the M_2 elevation and velocity signals are used to obtain an error estimate and to quantify spurious modes.

3.2. Results

Model output generated by each solution method on the 6eq grid with the coarsest nodal spacing (50 000 ft) is presented in Figures 5–7. The remaining grids show similar results and

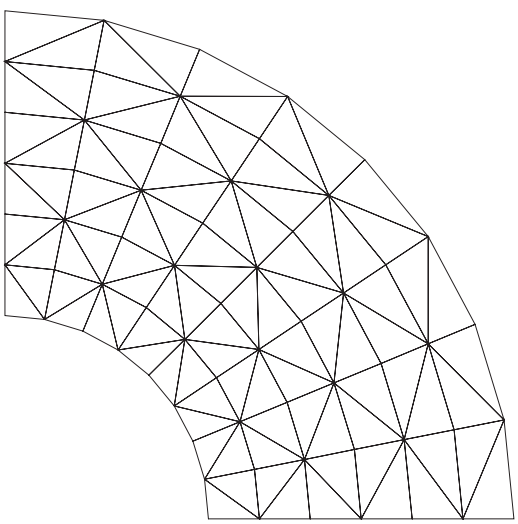

Figure 4. 4–8 grid configuration.

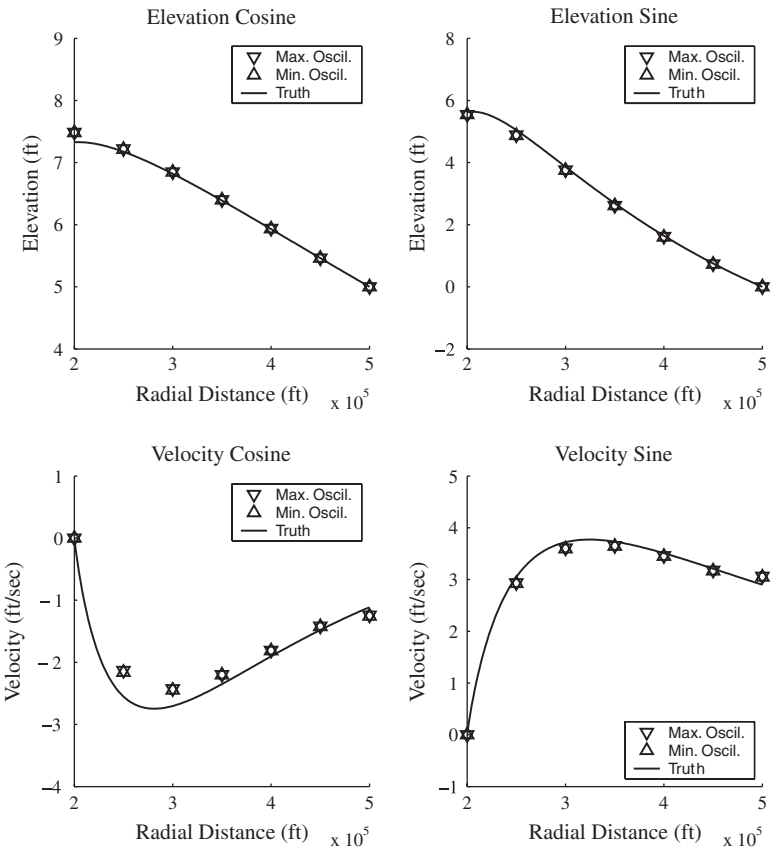

Figure 5. GWCE results on 6eq with $h = 50\,000$ ft.

are omitted for brevity. The four M_2 solution components from the harmonic analysis are shown in each figure, and each subplot gives a comparison of numerical results to the 'truth' solution generated using the GWCE method with a grid spacing of 1562.5 ft. The numerical results are given every 50 000 ft, corresponding to the radial locations where nodes are aligned. The two opposing triangles show the adjacent nodal values that are most different at the specified radial distance. Any difference between the triangular marks shows the size of the largest node-to-node oscillation along that radius, a measure of oscillation in the $\Delta\theta$ direction. The GWCE method (Figure 5) matches the 'truth' solution although some small differences do exist, as seen in velocity response toward the shallow end of the harbour. It appears that the essential boundary condition on the velocity solution in the momentum equation along with the no-normal flux enforcement in the continuity equation is introducing error at the land boundary. Also, the velocity solution appears to be inaccurate on the elevation forcing boundary due to the first-order accurate boundary condition treatment within the momentum equation. Note that no discernible oscillations exist, a basic characteristic of GWCE solutions. The DG method (Figure 6) also matches the 'truth' solution very well. Slight oscillations are

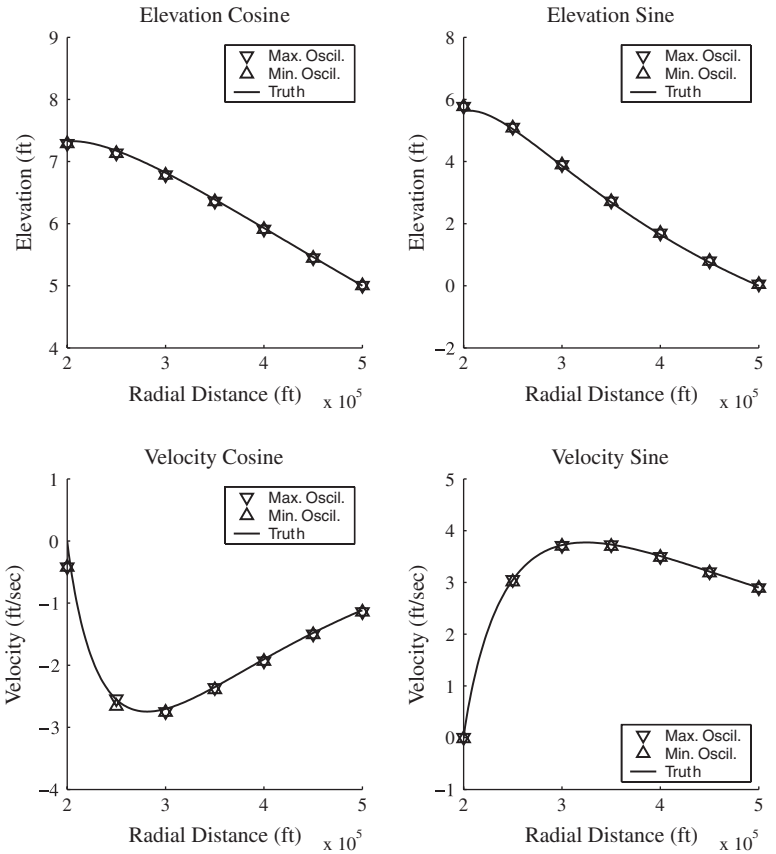

Figure 6. DG results on 6eq with $h = 50\,000$ ft.

observed in the velocity signal at the shallow end of the harbour, perhaps the result of the elementally based, discontinuous nature of the DG solution. Also, while there are small errors at the boundaries (particularly at the high-gradient inner boundary) due to a weak boundary enforcement, the DG solution most closely matches the 'truth' solution in near-boundary regions. This indicates its second-order boundary implementation is not degrading solution quality on the interior, which does not appear to be true with the boundary implementation of the other methods. Figure 7 shows results from the DG/CG method, which exhibits errors at the shallow end of the harbour (as does the GWCE solution, which applies the same boundary condition on velocity response there). The essential boundary condition on velocity at the inner no-normal flow boundary affects the quality of the elevation response. The weak boundary condition on elevation on the elevation-specified forcing boundary does not appear to degrade the solution, similar to the DG response. Note that oscillations in the $\Delta\theta$ direction are minimal, although a slight oscillation exists between adjacent radii and can be noted in the velocity sine result.

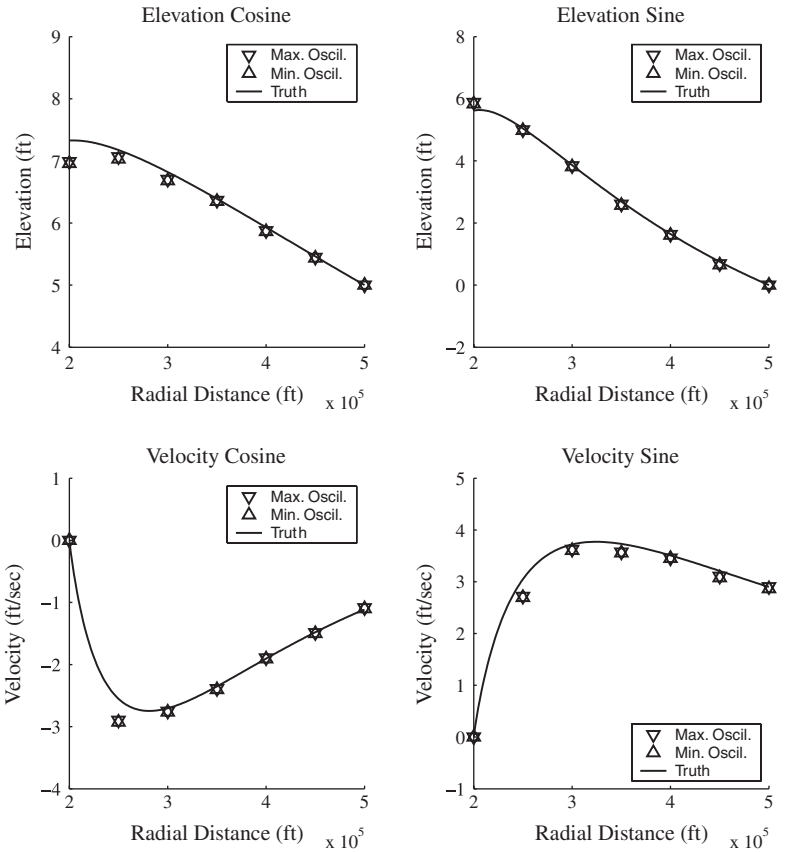

Figure 7. DGCG results on 6eq with $h = 50\,000$ ft.

Error estimates are generated for all four solution components by comparing solution harmonic output to the 'truth' solution at each nodal location. The root-mean-square (RMS) of these nodal errors is then calculated as described in Equation (13), where e is the difference between the 'truth' and computed solutions at each node and n is the number of nodes.

$$\mathrm{RMS} = \left[\sum_{i=1}^{n} e_i^2 \Big/ n \right]^{1/2} \tag{13}$$

It should be noted that the DG and DG/CG algorithms project elemental-based results onto adjacent nodes for analysis. The RMS error is calculated for all four levels of grid resolution to study the convergence behaviour of each method. In order to estimate each convergence rate, a line is fitted to the error data in a least-squares sense, and the slope of this line on the log–log plot is reported in the legend. These error analyses are taken within the asymptotic range, as confirmed by Richardson-based error estimates which are consistent on all grid spacings. We also calculate the RMS error over a subset of nodes on the interior of the domain in order to limit the influence of low-order boundary conditions on convergence behaviour. This

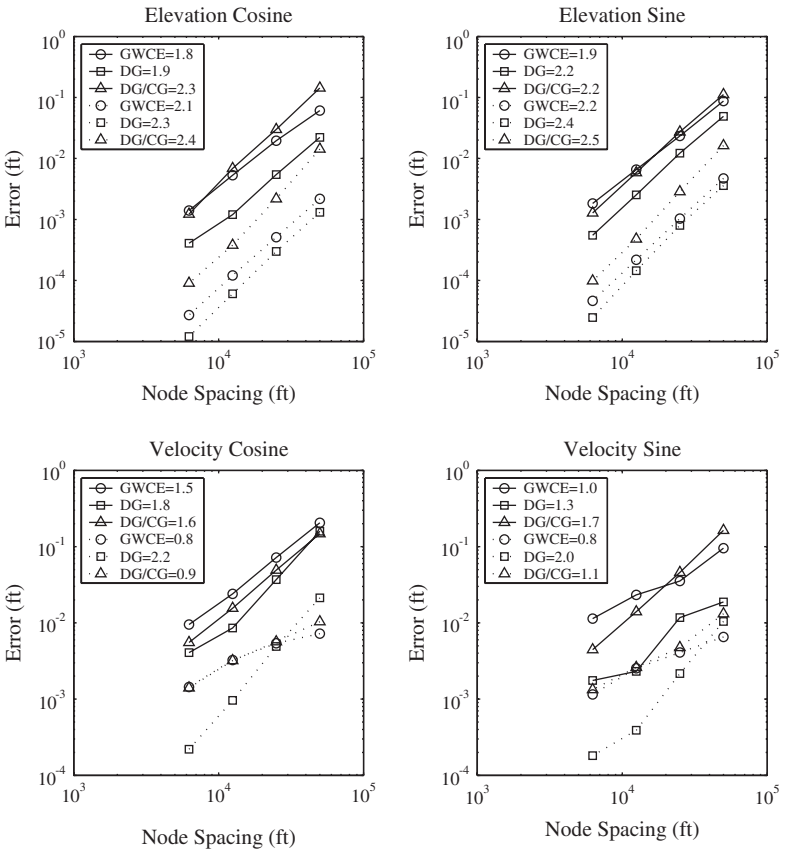

Figure 8. 6eq: RMS errors (—) and oscillations (···) over all nodes.

subset is defined as all nodes greater than 50 000 ft from the boundary, which corresponds to the interior nodes for the coarsest grid.

Oscillations in the θ direction for each solution have been calculated. These node-to-node oscillations are determined by comparing the solution at each node along a radius to values at its neighbours. A measure of the oscillations for each method is then generated by computing the RMS of the oscillations. As with the error evaluations, the RMS of the oscillations is calculated over all nodes and over the interior set of nodes described above in order to examine boundary condition effects.

6eq grid configuration. Global convergence plots of RMS error and RMS oscillation versus grid spacing for all solution components of the GWCE, DG, and DG/CG methods are shown in Figure 8. These can be compared to convergence plots at locations on the interior away from the boundary in Figure 9 in order to examine the effect of boundary implementation. These are calculated only over nodes 50 000 ft or more from any boundary.

RMS errors in both figures indicate that the DG method is generally the most accurate on the 6eq grid, while the GWCE and DG/CG solutions are less accurate but are similar to each

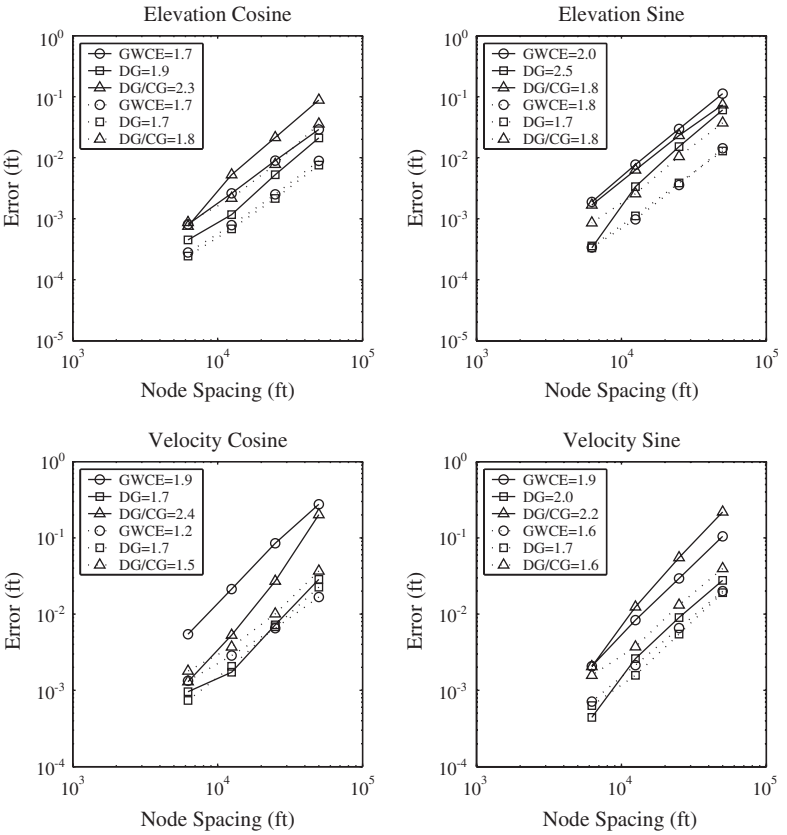

Figure 9. 6eq: RMS errors (—) and oscillations (···) over interior nodes.

other. RMS errors are often smaller over the interior, where lower accuracy boundary treatment effects are removed from the RMS calculation. Furthermore, convergence of RMS error on the interior is close to second order for all three solutions. This often represents an increase in the velocity solution convergence rate as compared to over the entire domain, although elevation solution convergence rates calculated over the interior are similar to rates calculated over the entire domain. In particular, GWCE and DG/CG velocity solution components converge at an increased rate on the interior. Recall that at the elevation forcing boundary, the velocity computation is first-order accurate for both of these methods. This first-order error affects the convergence rate of the velocity solution, preventing it from reaching second order. The DG solution experiences little difference in the convergence behaviour of its RMS error whether over the interior or all nodes, confirming that lower order boundary effects are not problematic in the DG method. There is an exception in the DG velocity sine RMS error convergence, which increases from 1.3 to 2.0 on the interior.

Comparisons of RMS oscillations for all methods shows that oscillations are generally largest for the DG/CG solution and are comparable between the DG and GWCE solutions. The only exception is the GWCE RMS oscillations for velocity calculated over the entire domain,

which are larger than those from the DG solution and compare closely to the RMS oscillations in the DG/CG velocity solutions. Note that these GWCE velocity solutions are affected by the first-order boundary treatment at the elevation boundary as well as a over-constrained boundary condition implementation at velocity boundaries. These boundary condition effects may impart oscillations into the velocity solution.

RMS oscillations are generally smaller than RMS errors over the entire domain by one-to-two orders of magnitude. However, when only interior nodes are considered, the RMS oscillation can exceed the RMS error, as the RMS oscillations on the interior subset of nodes tend to be larger than when all nodes are included. This suggests that boundary conditions have oscillation-suppression tendencies in the vicinity of the boundary. This is likely related to the fact that essentially enforced elevation and velocity values are by nature oscillation-free.

Oscillation reduction with respect to decreasing node spacing is between first and second order for all methods. Elevation RMS oscillation convergence rates on the interior are lower than on the entire domain for all methods, likely related to oscillation suppression at the elevation-specified boundary condition. For the GWCE and DG/CG methods (which both impose a first-order response in the velocity solution at elevation-specified boundaries), velocity RMS oscillation convergence rates are somewhat greater on the interior, where boundary effects are minimized. This implies that the low-order boundary treatments are limiting reduction in oscillation size. Conversely, the DG method imposes weak boundary conditions through the Roe flux onto both the elevation and velocity fields. The DG velocity field has a modest decrease in its RMS oscillation convergence rate as does its elevation field on the interior of the domain.

6b grid configuration. Convergence behaviour on the 6b grid has been calculated as was done with the 6eq grid. Figure 10 shows the RMS errors and RMS oscillations calculated over all nodes, while the convergence behaviour on the set of interior nodes is shown in Figure 11.

Examination of RMS errors for each solution shows that there are many similarities to the results found with the 6eq grid. In fact, the DG and GWCE error curves are almost identical to those for grid 6eq. The DG method again has the most accurate solution, but on the 6b grid, the GWCE method is generally more accurate than the DG/CG method. Again, RMS error is often smaller over the interior than over the entire domain, since boundary effects are minimized. First we compare convergence behaviour on 6b to 6eq using RMS error over the entire domain. All methods have convergence rates between first and second order based upon RMS errors calculated over the entire domain. The GWCE method again exhibits smooth, consistent convergence rates close to second order for elevation solution components, but again velocity convergence rates, particularly for the sine component, show reduced convergence due to the boundary treatment. The DG results are very similar to those from the 6eq grid, showing a convergence rate close to 2 for all solution components. Convergence rates for the DG/CG method, however, are noticeably different from the 6eq grid. While most results on the 6eq grid are close to second order, on the 6b grid the convergence rates are generally in the range of 1–1.5. When only considering the interior, again the convergence rates for all methods are generally closer to second order. The GWCE method demonstrates noticeable improvement in velocity convergence rates, which now are close to 2. The DG method does not experience much difference in convergence behaviour between the interior and entire domain RMS errors, as was seen in the 6eq results. Finally, the DG/CG results do not show improvement and are comparable to convergence rates generated over all nodes. It appears that the 6b grid configuration hampers DG/CG convergence.

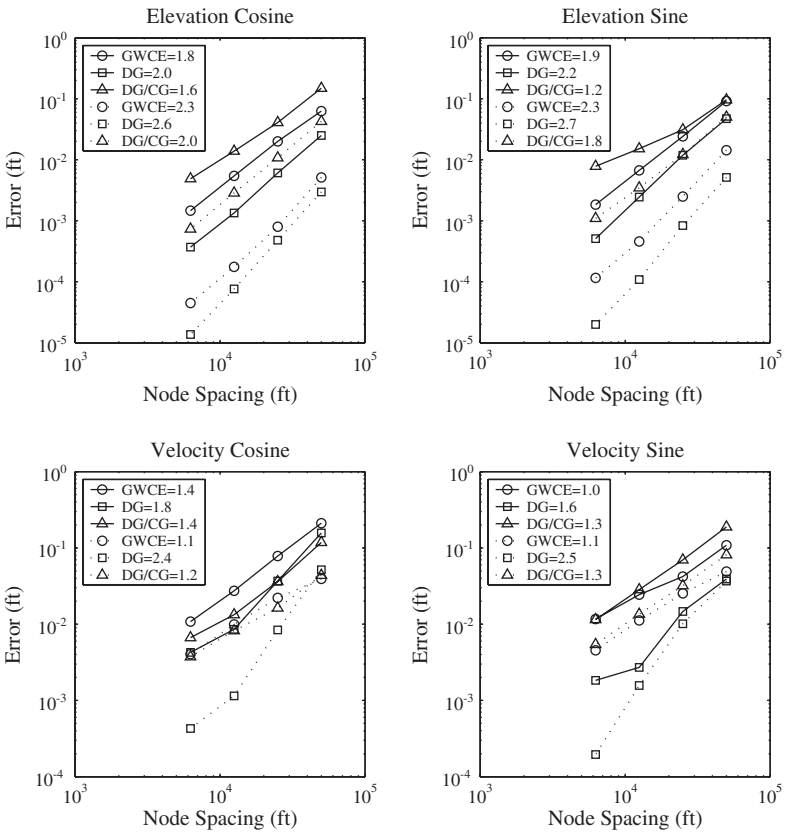

Figure 10. 6b: RMS errors (—) and oscillations (···) over all nodes.

Oscillations from the 6b simulations have been calculated as before. RMS oscillations in the DG method are comparable to the RMS oscillations from the 6eq grid; however, the GWCE RMS oscillations have increased somewhat and the DG/CG RMS oscillations have increased dramatically. The DG/CG solution exhibits the largest RMS oscillations, which over the interior set of nodes can be almost two orders of magnitude larger than DG RMS oscillations, which are generally the smallest. The size of RMS oscillation seems to correspond to the RMS error for each method since over the interior nodes the values tend to be quite close. The larger DG/CG RMS oscillations over the interior seem to correlate to its larger errors. Oscillations on the interior subset of nodes are larger than when examining all nodes for the 6b grid, as was found in the 6eq results. Elevation RMS oscillation convergence rates on the interior are less than those on the entire domain, as in the 6eq solutions. Also, GWCE velocity RMS oscillations convergence rates are greater on the interior (as with the 6eq configuration). The DG/CG solution does not experience such an increase for the 6b grid configuration, however. The DG solution experiences a more dramatic reduction in velocity RMS oscillation convergence rates than on the 6eq grids, as they drop from greater than second order to nearly first.

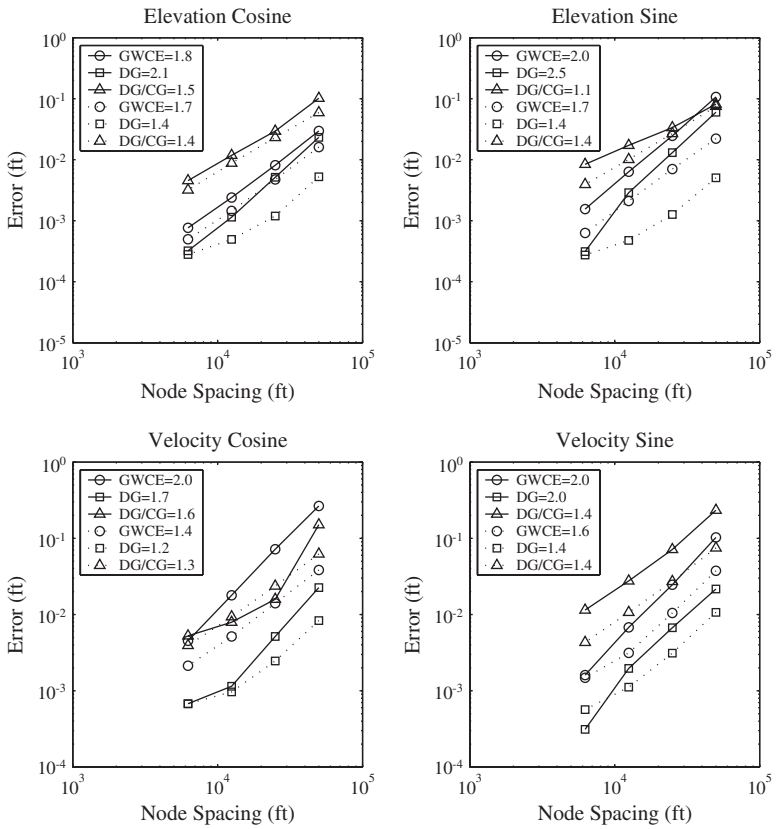

Figure 11. 6b: RMS errors (—) and oscillations (···) over interior nodes.

4–8 grid configuration. The convergence behaviour of all methods on the 4–8 grid is shown in Figure 12 and the convergence behaviour of these methods on the interior nodes of the 4–8 grid is shown in Figure 13.

RMS errors for the DG method are again the smallest, and the GWCE and DG/CG RMS errors are comparable. The RMS errors on the interior remove lower order boundary effects as with the 6eq and 6b grids, and therefore are smaller than the RMS errors over all nodes. RMS error values and convergence rates for all methods on the 4–8 grid are closely comparable to those found for the 6eq grid configuration, and are close to second order over the interior nodes. Recall that DG/CG convergence was hindered on 6b; 4–8 convergence rates and error levels are close to 6eq values. The effects of the one-sided, first-order boundary treatment of momentum equation is readily identified in the GWCE and DG/CG velocity RMS errors, which converge at a higher rate on the interior. The DG method does not show much difference in convergence behaviour between RMS errors over the entire domain or the interior, indicating its boundary condition treatment does not degrade solution quality.

Oscillations from the 4–8 grid simulations have been determined as before, and the results show the 4–8 grid configuration suffers from the largest RMS oscillations of all grids. In fact, on the 4–8 grid the methods show RMS oscillations that are larger than the RMS

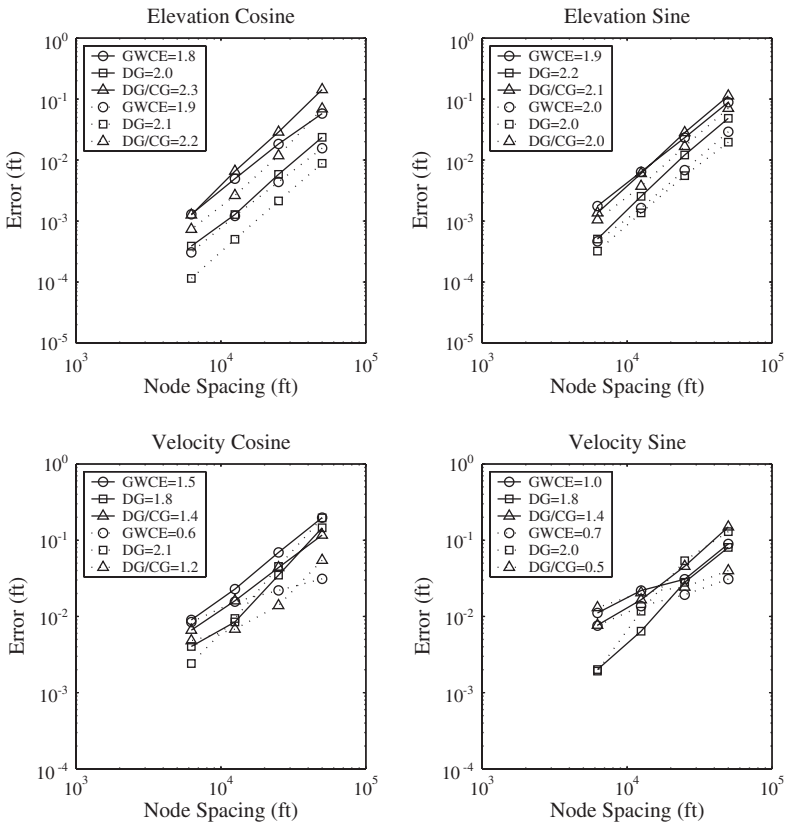

Figure 12. 4–8: RMS errors (—) and oscillations (···) over all nodes.

errors at high resolution. The DG continues to exhibit the smallest RMS oscillations and the DG/CG the highest, but the differences are small. As for the previous grid configurations, elevation RMS oscillation convergence rates decrease on the interior as the effects of the low oscillation boundary nodes are excluded. This decrease also holds true for the DG velocity RMS oscillation convergence rates, as was found earlier. The GWCE and DG/CG velocity RMS oscillation convergence rates are higher on the interior, as they were before, due to the removal of possibly over-constrained, oscillatory velocity solutions at the boundary.

3.3. Computational efficiency

Analysis of computational efficiency for all three numerical methods is performed in order to give a full comparison between the methods. Differences in discretization strategy between the continuous and DG methodologies lead to differences in the number of degrees of freedom and thus the number of operations per time step. Each strategy discretizes the three variables (ξ and $\mathbf{u}$) differently; in this paper we consider linear spatial approximations for all methods. The CG-based GWCE solution discretizes the variables on each node (with N nodes per grid) for a total of $3N$ degrees of freedom. The DG method discretizes each variable by constructing linear approximations elementally (with M elements per grid) which results in

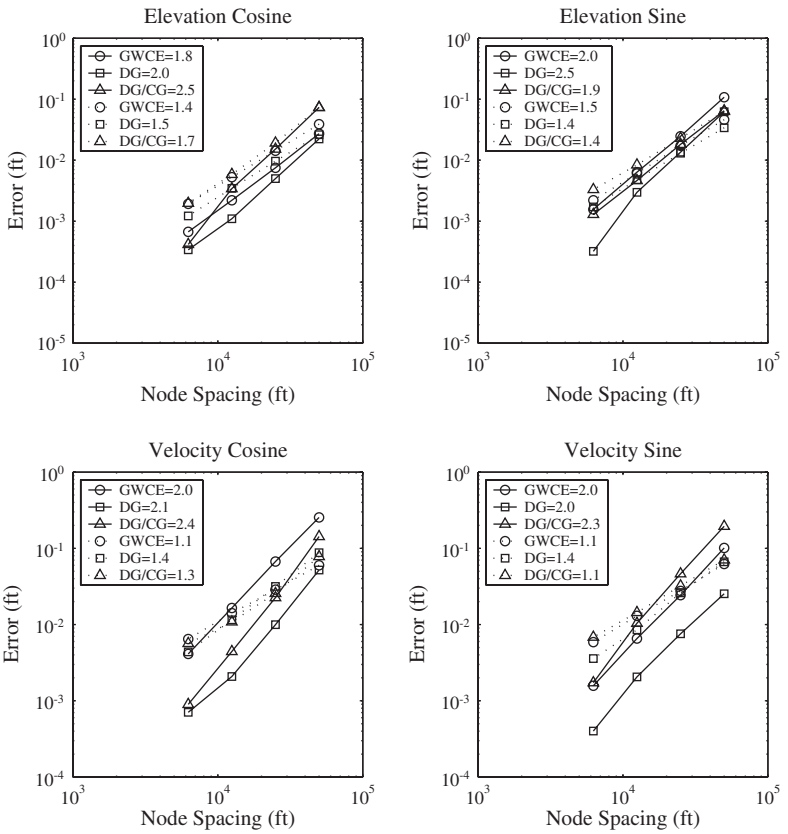

Figure 13. 4–8: RMS errors (—) and oscillations (···) over interior nodes.

$9M$ degrees of freedom. The DG/CG algorithm is a combination of these approaches. The continuity equation discretizes ξ elementally which leads to $3M$ degrees of freedom, and the velocity field $\mathbf{u}$ is discretized nodally, which generates $2N$ degrees of freedom, for a total of $3M+2N$. The number of triangular elements in a grid can be estimated as twice the number of nodes for typical grids ($M=2N$). Based upon the degrees of freedom operated on, the GWCE method ($3N$) will be most efficient, DG most costly ($18N$), and DG/CG ($8N$) in between. However, there are other factors affecting computational cost. The GWCE method solves a more complex wave-type equation, increasing the number of terms by a factor of three to nine depending upon the non-linear terms evaluated as compared to the primitive continuity equation. This increases the cost per time step by an average of $6N$–$9N$. DG employs an explicit second-order Runge–Kutta time-stepping procedure which involves two solutions per time step, raising cost to $36N$. DG/CG employs the Runge–Kutta procedure on the continuity equation ($12N$) and then solves the momentum equations using the same procedure as the GWCE method ($2N$), leading to a total of $14N$ operations per time step. Once time stepping is taken into account it can be seen that the DG/CG method avoids some of the cost of the DG solution procedure. A range of additional factors will also affect solution cost: the GWCE

itself requires the solution of a system of equations; integration and cost vary dramatically between the solutions; the DG and DG/CG methods require the solution of the Riemann problem; the DG and DG/CG methodologies employ a slope-limiting procedure over each element's edge for the elevation field; the DG/CG method requires a simple projection of the local elementally expanded elevation solution into the continuous, nodally based space W_h; and the GWCE coding has been extensively optimized while this is not the case for the DG and DG/CG solutions. Finally, we have assumed that all methods can employ the same time step, although in practice the explicit Runge–Kutta scheme in DG and DG/CG may require a smaller time step than the GWCE solution.

In order to verify these cost estimates, a series of runs were done to document run times for each method. Three versions of the 6b grid were run, with resolutions of 50 000, 25 000, and 12 500 ft in the direction of propagation, and all tests employed a 2.5 s time step. The results verify the relative cost estimates of the methods. The timing runs were done on a SUN Blade 2000 with a single 1.015 GHz CPU and 1 GB memory running Solaris 8 and SUN's native compilers. Recorded wall clock run times are shown in Table I and are plotted against the number of nodes in Figure 14. The results show that all methods increase run

Table I. Run time (min).

Grid	Nodes	GWCE	DG	DG/CG
1	63	8	33	13
2	221	26	134	49
3	825	106	480	202

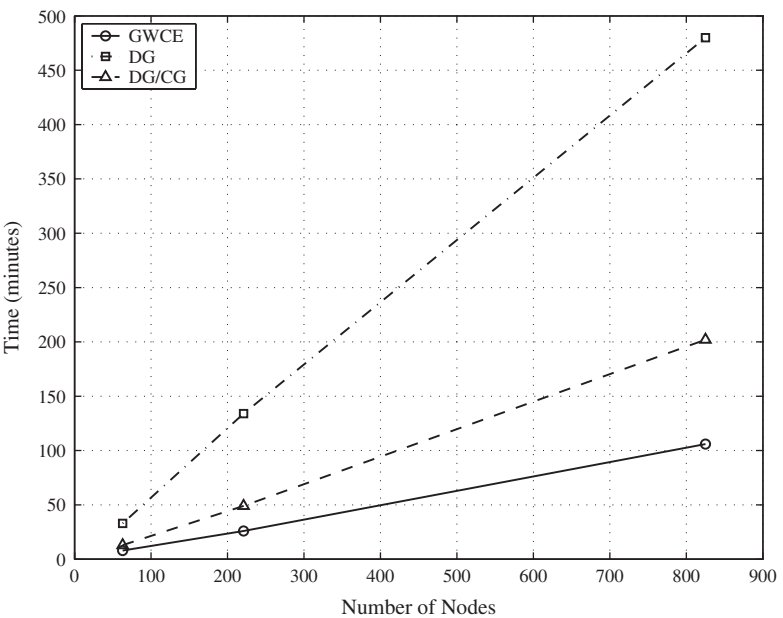

Figure 14. Run time.

time linearly with the number of nodes. Furthermore, the GWCE method is shown to be approximately twice as efficient as DG/CG, which itself is more than twice as efficient as DG. These results confirm that the increased degrees of freedom of DG methodologies do increase cost as compared with CG methods.

4. CONCLUSIONS

A novel numerical approach to modelling the SWE has been presented and compared to existing methods. The coupled continuous/discontinuous (DG/CG) Galerkin finite element method is a mass-conserving, flux-continuous numerical scheme that is not plagued by spurious modes or instabilities. Solutions from the GWCE, DG, and DG/CG algorithms are compared on the quarter annular test case using three different grid configurations. The DG method is shown to be the most accurate, while the GWCE method may only be slightly more accurate than the DG/CG method. Once boundary condition effects are removed, the convergence rate of RMS errors for all methods is second order, although the DG method does not experience much change in its convergence rate whether boundary condition effects are considered or not, indicating its boundary condition treatment is not degrading accuracy and is second order. However, the RMS error is often less when only interior nodes are included in the RMS calculation for all methods. It is observed that the GWCE and DG/CG methods suffer from a low-order approximation of the pressure gradient term in the momentum equation at elevation boundaries, which degrades the accuracy of the velocity solution near the forcing boundary.

Examination of node-to-node oscillations along a constant radius line shows that DG tends to have the smallest oscillations and DG/CG the largest. The RMS oscillation tends to increase on the interior of the domain because boundary nodes are removed from the RMS calculation and these appear to minimize oscillations, as they are constrained by the boundary condition. Furthermore, elevation RMS oscillation convergence rates decrease on the interior because the oscillation-free boundary nodes are not considered. This effect also holds true for the DG velocity solution, which suppresses oscillations near the boundary due to the numerical boundary flux integral term on both the continuity and momentum equations (and thus both the elevation and velocity fields). However, velocity RMS oscillation convergence rates increase on the interior for the GWCE and DG/CG solutions, perhaps due to an over-constrained essential velocity boundary condition implementation at no-normal flow velocity boundaries.

Computational efficiency of the three schemes has been tested over a series of grids. The GWCE method is shown to be most efficient, with the DG/CG being less and the DG method most costly. This is expected considering that DG methodologies increase the number of degrees of freedom, and run times bear this out. The cost comparison, however, is based on the number of elements and not the overall accuracy of the methods.

In conclusion, it can be seen that there are advantages and disadvantages to each of the three methods. The GWCE solution has been widely used and appropriately so; it is an efficient numerical scheme that is accurate (although less than DG), converges at second order, and suppresses spurious oscillations. However, it suffers from a complex structure that is difficult to analyse, is dependent upon the selection of the numerical weighting parameter τ_0, and is known to suffer mass imbalances as well as perform poorly for highly non-linear flows. It is not an appropriate algorithm for problems with non-smooth velocity profiles as it does not

have the capability to handle these highly advective conditions. The DG method addresses many of its flaws (it satisfies continuity, can handle highly non-linear flows including shock conditions, is easily coded, and has been shown to be highly accurate). However, it is a costly approach to solving the governing equations. The novel DG/CG method is a combination of these two approaches. It provides a mass conserving solution while reducing the cost of the full DG implementation. However, it is shown to be somewhat less accurate than DG as well and is susceptible to oscillations which limits its capability for cases with non-smooth velocity profiles, an area in which the GWCE is deficient but the full DG method bring advantageous.

Finally, we note the use of equilateral finite elements (the 6eq grid configuration) is advantageous, as it exhibits the smallest errors and oscillations. Conversely, triangular elements composed of bisected quadrilaterals (the 6b grid configuration) appear to reduce the accuracy, especially with the DG/CG solution.

ACKNOWLEDGEMENTS

This research was supported by NSF grant DMS-0107247. This research was also supported by the U.S. Army Engineer Research and Development Centre under contract DACW 42-00-C-0006.

REFERENCES

1. Weiyan T. *Shallow Water Hydrodynamics*, Elsevier Oceanography Series, vol. 55. Elsevier: Amsterdam, 1992.
2. Westerink JJ, Luettich RA, Baptista AM, Scheffner NW, Farrar P. Tide and storm surge predictions using a finite element model. *Journal of Hydraulic Engineering* 1992; **118**:1373–1390.
3. Blain CA, Westerink JJ, Luettich RA. The influence of domain size on the response characteristics of a hurricane storm surge model. *Journal of Geophysical Research* 1994; **99**(C9):18467–18479.
4. Lynch DR, Gray WG. A wave equation model for finite element computations. *Computers and Fluids* 1979; **7**:207–228.
5. King IP, Norton WR. Recent application of RMA's finite element models for two-dimensional hydrodynamics and water quality. In *Finite Elements in Water Resources II*, Brebbia CA, Gray WG, Pinder GF (eds). Pentech Press: London, 1978.
6. Kawahara M, Hirano H, Tsuhora K, Iwagaki K. Selective lumping finite element method for shallow water equations. *International Journal for Numerical Methods in Engineering* 1982; **2**:99–112.
7. Szymkiewicz R. Oscillation-free solution of shallow water equations for nonstaggered grid. *Journal of Hydraulic Engineering* 1993; **119**:1118–1137.
8. Zienkiewicz OC, Ortiz P. A split-characteristic based finite element model for the shallow water equations. *International Journal for Numerical Methods in Fluids* 1995; **20**:1061–1080.
9. Kinnmark IPE. The shallow water wave equations: formulation, analysis, and application. *Ph.D. Thesis*, Department of Civil Engineering, Princeton University, 1984.
10. Gray WG, Drolet J, Kinnmark IPE. A simulation of tidal flow in the southern part of the North Sea and the English Channel. *Advances in Water Resources* 1987; **10**:131–137.
11. Gray WG. A finite element study of tidal flow data for the North Sea and English Channel. *Advances in Water Resources* 1989; **12**:143–154.
12. Foreman MGG. An analysis of the wave equation model for finite element tidal computations. *Computational Physics* 1983; **52**:290–312.
13. Foreman MGG. A comparison of tidal models for the southwest coast of Vancouver Island. In *Computational Methods in Water Resources*: *Proceedings of the VII International Conference*, *MIT*, Celia MA (ed.), vol. 2. Elsevier: Amsterdam, 1988.
14. Luettich RA, Westerink JJ, Scheffner NW. ADCIRC: an advanced three-dimensional circulation model for shelves, coasts and estuaries, Report 1: theory and methodology of ADCIRC-2DDI and ADCIRC-3DL. *Dreding Research Program Technical Report DRP-92-6*, *U.S. Army Engineers Waterways Experiment Station*, *Vicksburg*, *MS*. U.S. Army Corps of Engineers: Washington, DC, 1992.
15. Werner FE, Lynch DR. Field verification of wave equation tidal dynamics in the English Channel and southern North Sea. *Advances in Water Resources* 1987; **10**:115–130.
16. Werner FE, Lynch DR. Harmonic structure of English Channel/Souther Bight tides from a wave equation simulation. *Advances in Water Resources* 1987; **12**:121–142.

17. Blain CA, Westerink JJ, Luettich RA. Grid convergence studies for the prediction of hurricane storm surges. *International Journal for Numerical Methods in Fluids* 1998; **26**:369–401.
18. Kolar RL, Westerink JJ, Cantekin ME, Blain CA. Aspects of nonlinear simulations using shallow water models based on the wave continuity equation. *Computers and Fluids* 1994; **23**(3):523–538.
19. Westerink JJ, Luettich RA, Kolar RL. Advances in finite element modeling of coastal ocean hydrodynamics. In *11th International Conference on Computational Methods in Water Resources*, Aldama A (ed.), vol. 2. Computational Mechanics Publications: Southampton, U.K., 1996.
20. Chippada S, Dawson CN, Martínez ML, Wheeler MF. Finite element approximations to the system of shallow water equations, Part I: Continuous time a priori error estimates. *SIAM Journal on Numerical Analysis* 1998; **35**:692–711.
21. Chippada S, Dawson CN, Martínez ML, Wheeler MF. Finite element approximations to the system of shallow water equations, Part II: Discrete time a priori error estimates. *SIAM Journal on Numerical Analysis* 1998; **36**(1):226–250.
22. Alcrudo F, Garcia-Navarro P. A high-resolution Godunov-type scheme in finite volumes for the 2d shallow-water equations. *International Journal for Numerical Methods in Fluids* 1993; **16**:489–505.
23. Chippada S, Dawson CN, Martínez ML, Wheeler MF. A Godunov-type finite volume method for the system of shallow water equations. *Computer Methods in Applied Mechanics and Engineering* 1998; **151**:105–129.
24. Aizinger V, Dawson C. Discontinuous Galerkin methods for two-dimensional flow and transport in shallow water. *Advances in Water Resources* 2002; **25**:67–84.
25. Giraldo FX, Hesthaven JS, Warburton T. Nodal high-order discontinuous Galerkin methods for the spherical shallow water equations. *Journal of Computational Physics* 2002; **181**:499–525.
26. Schwanenberg D, Harms M. Discontinuous Galerkin finite element method for transcritical two-dimensional shallow water flows. *Journal of Hydraulic Engineering* 2004; **130**(5):412–421.
27. Eskilsson C, Sherwin SJ. A triangular spectral/hp discontinuous Galerkin method for modeling 2D shallow water equations. *International Journal for Numerical Methods in Fluids* 2004; **45**(6):605–623.
28. Dawson C. Conservative, shock-capturing transport methods with nonconservative velocity approximations. *Computational Geosciences* 1999; **3**:205–227.
29. Cockburn B, Shu CW. The Runge–Kutta local projection P^1-discontinuous Galerkin method for scalar conservation laws. *RAIRO Modélisation Mathématique et Analyse Numérique* 1991; **25**:337–361.
30. Cockburn B, Shu CW. TVB Runge–Kutta local projection discontinuous Galerkin finite element method for scalar conservation laws II: general framework. *Mathematics of Computation* 1989; **52**:411–435.
31. Cockburn B, Lin SY, Shu CW. TVB Runge–Kutta local projection discontinuous Galerkin finite element method for conservation laws III: one dimensional systems. *Journal of Computational Physics* 1989; **84**:90–113.
32. Cockburn B, Hou S, Shu CW. TVB Runge–Kutta local projection discontinuous Galerkin finite element method for conservation laws IV: the multidimensional case. *Mathematics of Computation* 1990; **54**: 545–581.
33. Cockburn B, Shu CW. The Runge–Kutta discontinuous Galerkin finite element method for conservation laws V: multidimensional systems. *Journal of Computational Physics* 1998; **141**:199–224.
34. Bey KS, Oden JT. *hp*-version discontinuous Galerkin methods for hyperbolic conservation laws. *Computer Methods in Applied Mechanics and Engineering* 1996; **133**:259–286.
35. Baumann CE, Oden JT. A discontinuous hp finite element method for convection–diffusion problems. In *Computer Methods in Applied Mechanics and Engineering special issue on Spectral, Spectral Element, and hp Methods in CFD*, Ainsworth M, Karniadakis GE, Bernardi C (eds), vol. 175. 1999; 311–341.
36. Cockburn B, Shu CW. The local discontinuous Galerkin finite element method for convection–diffusion systems. *SIAM Journal on Numerical Analysis* 1998; **35**:2440–2463.
37. Cockburn B, Dawson C. Some extensions of the local discontinuous Galerkin method for convection–diffusion equations in multidimensions. In *Proceedings of the Conference on the Mathematics of Finite Elements and Applications*: *MAFELAP X*, Whiteman JR (ed.). Elsevier: Amsterdam, 2000.
38. Dawson C, Proft J. A priori error estimates for interior penalty versions of the local discontinuous Galerkin method applied to transport equations. *Numerical Methods for Partial Differential Equations* 2001; **17**(6): 545–564.
39. Wheeler MF. An elliptic collocation-finite element method with interior penalties. *SIAM Journal on Numerical Analysis* 1978; **15**:152–161.
40. Baker GA. Finite element methods for elliptic equations using nonconforming elements. *Mathematics of Computation* 1977; **31**:45–59.
41. Castillo P, Cockburn B, Perugia I, Schötzau D. An a priori error analysis of the local discontinuous Galerkin method for elliptic problems. *SIAM Journal on Numerical Analysis* 2000; **38**(5):1676–1706.
42. Oden JT, Babuška I, Baumann CE. A discontinuous hp finite element method for diffusion problems. *Journal of Computational Physics* 1998; **146**:491–519.
43. Rivière B, Wheeler MF, Girault V. Improved energy estimates for interior penalty, constrained and discontinuous Galerkin methods for elliptic problems, Part I. *Computational Geosciences* 1999; **3**:337–360.

44. Cockburn B, Karniadakis GE, Shu CW. The development of discontinuous Galerkin methods. In *First International Symposium on Discontinuous Galerkin Methods*, Cockburn B, Karniadakis GE, Shu CW (eds), Lecture Notes in Computational Science and Engineering, vol. 11. Springer: Berlin, 2000; 3–50.
45. Dawson C, Proft J. Discontinuous and coupled continuous/discontinuous Galerkin methods for the shallow water equations. *Computer Methods in Applied Mechanics and Engineering* 2002; **191**:4721–4746.
46. Blain CA, Massey TC. Application of a coupled discontinuous–continuous Galerkin finite element shallow water model to coastal ocean dynamics. *Ocean Modelling* 2005; **10**(3–4):283–315.
47. Durlofsky L, Engquist B, Osher S. Triangle based adaptive stencils for the solution of hyperbolic conservation laws. *Journal of Computational Physics* 1992; **98**:64–83.
48. Lynch DR, Gray WG. Analytical solutions for computer flow model testing. *Journal of the Hydraulics Division* (ASCE) 1978; **HY-10**:1409–1428.
49. Atkinson JH, Westerink JJ, Luettich RA. Two dimensional dispersion analysis of finite element approximations to the shallow water equations. *International Journal for Numerical Methods in Fluids* 2004; **45**(7):715–749.
50. Roache PJ. *Verification and Validation in Computational Science and Engineering*. Hermosa Publishers: Albuquerque, 1998.

